

ANALYSIS OF CLUMPS IN MOLECULAR CLOUD MODELS: MASS SPECTRUM, SHAPES, ALIGNMENT AND ROTATION

CHARLES F. GAMMIE AND YEN-TING LIN

Center for Theoretical Astrophysics, University of Illinois
1002 W. Green St., Urbana, IL 61801, USA; gammie@uiuc.edu, ylin2@astro.uiuc.edu

JAMES M. STONE AND EVE C. OSTRIKER

Astronomy Department, University of Maryland,
College Park, MD 20742 USA.; jstone@astro.umd.edu, ostriker@astro.umd.edu
Draft version November 15, 2018

ABSTRACT

Observations reveal concentrations of molecular line emission on the sky, called “clumps,” in dense, star-forming molecular clouds. These clumps are believed to be the eventual sites of star formation. We study the three-dimensional analogs of clumps using a set of self-consistent, time-dependent numerical models of molecular clouds. The models follow the decay of initially supersonic turbulence in an isothermal, self-gravitating, magnetized fluid. We find the following. (1) Clumps are intrinsically triaxial. This explains the observed deficit of clumps with a projected axis ratio near unity, and the apparent prolateness of clumps. (2) Simulated clump axes are not strongly aligned with the mean magnetic field within clumps, nor with the large-scale mean fields. This is in agreement with observations. (3) The clump mass spectrum has a high-mass slope that is consistent with the Salpeter value. There is a low-mass break in the slope at $\sim 0.5 M_{\odot}$, although this may depend on model parameters including numerical resolution. (4) The typical specific spin angular momentum of clumps is $4 \times 10^{22} \text{ cm}^2 \text{ s}^{-1}$. This is larger than the median specific angular momentum of binary stars. Scaling arguments suggest that higher resolution simulations may soon be able to resolve the scales at which the angular momentum of binary stars is determined.

Subject headings: ISM: clouds, ISM: Molecules, Magnetohydrodynamics: MHD, Methods: Numerical, Stars: Formation

1. INTRODUCTION

Star forming molecular clouds are observed to be highly inhomogeneous in molecular line emission and continuum absorption studies. They contain relatively empty voids as well as dense “clumps” and denser “cores” within these clumps. One expects that stars will form in the densest parts of molecular clouds, and clumps are indeed correlated with young stars (Williams et al. 1994; Phelps & Lada 1997). Clumps (or cores) therefore appear to be the immediate precursors of clusters, small groups, or individual stars in the interstellar medium; they constitute the initial conditions for star formation.

Theoretical models of diffuse precursors to stars were, until recently, confined to static or quasi-static equilibrium models. Mouschovias (1976) constructed numerical models of static, axisymmetric, magnetically supported, self-gravitating equilibria (see also: Barker & Mestel 1996; Li & Shu 1996; Galli & Shu 1993; Baureis et al. 1989; Tomisaka et al. 1988a,b; Mestel & Ray 1985). These models do not include the effects of turbulence. Quasi-static models, in which the effects of turbulence are included as an effective pressure, fixed by an assumed equation of state, have been constructed by Lizano & Shu (1989) (see also Myers & Fuller 1992; McLaughlin & Pudritz 1996; Curry & McKee 2000).

Both the static and quasi-static approach have weaknesses. The static, magnetically supported models predict oblate cores, flattened perpendicular to the mean magnetic field (but see Fiege & Pudritz 2000). Observations yield shapes apparently more consistent with prolate clumps (Myers et al. 1991; Ryden 1996), and little correlation be-

tween field direction and clump shape (Heiles et al. 1993). They also do not include the effects of turbulent velocities, which are directly observed through their contribution to the linewidth of molecular line transitions even at small spatial scales (e.g. Goodman et al. 1998).

The quasi-static models, on the other hand, account for turbulent velocities by invoking a steady turbulent pressure. It not immediately apparent that supersonic turbulence like that observed in molecular clouds would act to prevent collapse, since the turbulence itself leads directly to compressions that might accelerate collapse. Recent numerical simulations show, furthermore, that supersonic magnetized turbulence dissipates in a dynamical time (Stone et al. 1998; Mac Low 1999). If these simulations correctly represent conditions in molecular clouds then even an approximate steady state cannot be achieved unless momentum is continually injected into the cloud.

Three-dimensional (3D), dynamic numerical models of molecular clouds have recently become practical (e.g., Vázquez-Semadeni et al. 1998 and the references therein; Stone et al. 1998; Mac Low 1999; Padoan & Nordlund 1999; Pichardo et al 2000; Ostriker et al. 2001). They do not impose a high degree of symmetry on the cloud and allow a largely self-consistent treatment of turbulence, although due to numerical diffusion they have a much lower effective Reynolds numbers than real interstellar clouds. In this paper we will study the density concentrations that arise self-consistently from self-gravitating turbulence in a set of numerical models.

Before we proceed, it is worth discussing the limitations of the model and the approximations that we use.

Our models integrate the equations of isothermal, compressible, self-gravitating, ideal magnetohydrodynamics (MHD). The isothermal approximation is used because realistic, time-dependent heating and cooling that treats the transfer of line radiation out of the cloud is, at present, out of numerical reach (but see Juvella et al. 2001). The model is fully self-gravitating, however, we use periodic boundary conditions in our solution of the Poisson equation. This distorts the gravitational field from what it would be in an isolated cloud by introducing additional tidal forces (although real clouds are not isolated, tidal forces are smaller). The numerical model is “ideal” in the sense that we do not include any explicit physical diffusion coefficients. All dissipation occurs in shocks, where it is captured by an artificial viscosity, or via numerical diffusion at the grid scale. Thus we do not model physical diffusion processes such as ion-neutral drift. This is almost certainly important in the dense regions of clouds, but an accurate treatment of the ionization, particularly UV ionization, that would motivate dynamical studies of non-ideal clouds is also numerically out of reach.

This paper is organized as follows: In §2 we give our definition of a “clump.” In §3 we describe our numerical methods and tests and give a qualitative and quantitative description of the evolution of the runs. The clump mass spectrum is described in §4. The distribution of clump shapes is described in §5, the orientation of the clumps with respect to the local and global magnetic field is described in §6, and a discussion on the clump spin angular momentum is given in §7. A summary and comparison with earlier work is given in §8.

2. CLUMPS: DEFINITIONS

Our first task is to define a “clump.” Any definition is somewhat arbitrary, much as the designation “mountain”¹ is arbitrary in topography. The definition should be: (1) physically motivated; (2) related to definitions used by observers in molecular line studies of clouds; (3) simple to describe; (4) easy to apply. Ultimately we are motivated by the desire to characterize those dense regions in molecular clouds that turn into stars.

Myers (1999) adopted the following definitions: a region of size $\gtrsim 10$ pc over which mean hydrogen number density $n_{H_2} \sim 10^2 \text{ cm}^{-3}$ is called a “complex”, a region of size ~ 1 pc over which $n_{H_2} \sim 10^3 \text{ cm}^{-3}$ is termed a “clump” and a “core” refers to a region of size ~ 0.1 pc over which $n_{H_2} \sim 10^4 \text{ cm}^{-3}$. A complex is well sampled by the CO $J = 1 \rightarrow 0$ transition, a clump can be traced by the $J = 1 \rightarrow 0$ line of ^{13}CO while a core is traced by the $(J, K) = (1, 1)$ line of NH_3 . The choice of 10^4 cm^{-3} as the fiducial density has several advantages, e.g., some easily observable molecular lines have effective critical density of this order.

There are two frequently-applied algorithms for identifying clumps in molecular line data. Each begins with intensity data in two space plus one velocity coordinates ($l-b-v$ space). The first algorithm, GAUSSCLUMPS, uses a fitting procedure that removes objects with a constrained gaussian shape from the data (e.g. Stutzki & Güsten 1990); it is analogous to the CLEAN algorithm used in radio interferometry. The second algorithm, CLUMPFIND,

identifies intensity maxima in $l-b-v$ space (Williams et al. 1994), then assigns each “pixel” (i.e., each channel in a spectrum) to be a member of the clump associated with the nearest intensity maximum.

These algorithms all implicitly make the assumption that the velocity coordinate v is somehow related to the line of sight distance z , i.e. that widely separated material that happens to lie at the same velocity is not confused in projection. As we have previously shown using simulated data sets (Ostriker et al. 2001; see also Pichardo et al. 2000; Ballesteros-Paredes & Mac Low 2002), this assumption may frequently *not* be satisfied for moderate-density condensations, although for rarer high-density peaks it probably is. With a suitable source function and radiative transfer scheme, it is possible to generate simulated $l-b-v$ data cubes for molecular transitions with varying critical densities, and thus to ascertain exactly when v is expected to be a valid surrogate for z . We defer consideration of this interesting and important problem to a later publication.

For the present work, we take advantage of our direct access to all three spatial coordinates in simulated data to study clumps in the unprojected density field. We associate clumps with spatial maxima in the density in much the same way that CLUMPFIND associates clumps with maxima in the intensity. Our algorithm operates as follows. Find all density maxima \mathbf{r}_i . Then associate every zone \mathbf{r} that lies above a threshold density ρ_t with the nearest \mathbf{r}_i . Each \mathbf{r}_i , together with the surrounding material that lies above the threshold density, is then a clump.

This algorithm is easy to implement and explain. It has one parameter ρ_t . A potential problem is that the density may contain small variation near the density maxima (are the Grand Tetons one mountain, or three?). If these variations occur on the grid scale, they may be purely numerical in origin. We can test the degree to which these variations split up what would otherwise be single clumps by smoothing the density and picking \mathbf{r}_i to be maxima of the smoothed density. This introduces one additional parameter, the smoothing length Δ .

What is the relationship of the 3D clumps described here with those seen by observers, in projection? As mentioned above, preliminary work (Ostriker et al. 2001) indicates that projection effects can be important. In each section below we will apply the same clump analysis to both the column density and the density as a way of evaluating the importance of projection effects.

3. NUMERICAL METHOD, TESTS, AND RUN EVOLUTION

We evolve the equations of isothermal, self-gravitating, compressible, ideal MHD using a numerical method based on the ZEUS code (Stone & Norman 1992a,b). It is a time-explicit, operator-split finite difference algorithm on a staggered mesh. Density and internal energy are zone-centered, while velocity components live on zone faces. The magnetic portion of the code uses the “method of characteristics” to evolve the transverse components of the magnetic and velocity field in a manner that assures the accurate propagation of Alfvén waves. The magnetic field is represented by fluxes through zone faces; these fluxes are evolved using “constrained transport,” (Evans & Hawley

¹ Merriam-Webster: “a landmass that projects conspicuously above its surroundings and is higher than a hill.”

1988) which preserves the constraint $\nabla \cdot \mathbf{B} = 0$ to machine precision.

The gravitational acceleration is obtained by differencing the gravitational potential. The potential is calculated using a Fourier transform technique. The gravitational kernel is defined by $\phi_{\mathbf{k}} = 4\pi G \rho_{\mathbf{k}} / (\sum_i (2 \cos(k_i \Delta x_i) - 2) / (\Delta x_i)^2)$. This kernel ensures that the natural finite difference form of the Poisson equation is satisfied. Notice that in a periodic domain the Poisson equation becomes

$$\nabla^2 \phi = 4\pi G (\rho - \bar{\rho}). \quad (1)$$

Evidently the periodic boundary conditions alter the potential from what it would be in an isolated cloud. The difference is most pronounced away from density maxima. In regions with $\rho \gg \bar{\rho}$ the potential is less affected by the periodic boundary conditions. This can be verified by explicit construction of sheetlike equilibria, which we have done.

We use an isothermal equation of state $p = c_s^2 \rho$, $c_s^2 = \text{const}$. This models the effect of efficient heating and cooling, and is appropriate when the cooling time is much shorter than the dynamical time.

Numerical convergence is a serious concern for the calculations presented here, particularly for the case of clumps that are only a few zones in size. The self-gravitating isothermal MHD equations will, under a broad range of circumstances, evolve toward density singularities (i.e. stars) that are unresolved. Many aspects of “protostellar” turbulence, however, may be insensitive to the internal structure of small, high-density regions. Certainly this is the assumption on which our numerical investigation is undertaken. At a minimum, however, we must only measure quantities on well-resolved scales.

3.1. Initial and Boundary Conditions

This paper considers a set of three numerical models which differ in magnetic field strength. Several aspects of evolution and structure for the same three models have previously been investigated by Ostriker et al. (2001). Each model has a numerical resolution of 256^3 zones.

The models are evolved in a periodic cubic domain of length L . The initial density and magnetic field are uniform. The initial velocity field, $\delta \mathbf{v}$, is chosen to be a divergence-free Gaussian random field with power spectrum $v_k^2 \sim k^{-4}$. This slope is compatible with Larson’s law; see, e.g., Myers & Gammie (1999). The perturbations have $E_w \equiv \frac{1}{2} \int d^3x (\rho \delta v^2 + \delta B^2 / 4\pi) = 100 \rho L^3 c_s^2$, although initially $\delta B = 0$. No further perturbations are added over the course of the evolution; these are *decay* simulations.

An important parameter of the model is the strength of selfgravity. At fixed physical density and sound speed, this strength is directly related to the physical size of the model L . A suitable nondimensional parametrization is in terms of the “Jeans number” $n_J \equiv L/L_J$, where $L_J^2 = \pi c_s^2 / (G \bar{\rho})$. All models discussed here have $n_J = 3$.

A second parameter is the strength of the mean magnetic field, $\langle B_x \rangle$, where $\langle \rangle$ indicates a volume average. $\langle B_x \rangle$ cannot change over time because of the periodic

boundary conditions. A sense of the dynamical importance of the mean field may be had by first comparing $v_{A,x} \equiv \langle B_x \rangle / \sqrt{4\pi \bar{\rho}}$ to the sound speed c_s . Our models have $v_{A,x}/c_s = 1$ (“weak” field), $\sqrt{10}$ (“moderate” field), and 10 (“strong” field). The strong and moderate field cases are most consistent with observations (e.g. Crutcher 1999; but see Padoan & Nordlund 1999 for a different perspective).

One may also compare the mean field strength to that required to prevent gravitational collapse: $\langle B_x \rangle > 2\pi \bar{\rho} L \sqrt{G}$ (Tomisaka 1988a,b). In terms of our dimensionless parameters $v_{A,x}/c_s$ and n_J , this becomes $v_{A,x}/c_s > \pi n_J$. Models which satisfy this condition are *subcritical*, i.e., will never experience complete gravitational collapse, while systems which fail to satisfy it are *supercritical*.² In the present work, the strong field model is subcritical and the other two models are supercritical.

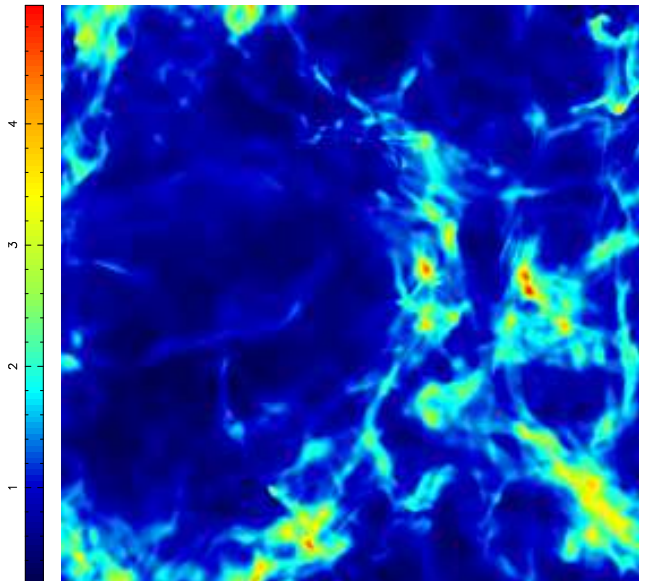


FIG. 1.— A color image of the surface density from snapshot **B** 9. The scale bar on the left shows column density relative to the mean column density.

3.2. Run Evolution

Once the model evolution is started, the initially incompressive velocity field distorts the initially uniform magnetic field. Since the magnetic field distortions are typically large, in the sense that $\delta B^2 / (8\pi) \gtrsim \rho c_s^2$, they couple strongly to compressive motions, and density variations result. Density variations also result from exchange of power between the compressive and incompressive parts of the velocity field; this would occur even in the absence of a magnetic field. Because the initial power spectrum of velocities we have chosen has v_λ , the velocity variation at a scale λ , varying as $\lambda^{1/2}$, and the timescale for a density variation to form is λ/v_λ , the density variations appear first at the smallest scales. Within a dynamical time, L/v_L , density variations have appeared at all scales and the flow is fully turbulent.

² The mass-to-flux ratio in our models is always constant. Relaxing this constraint introduces free functions, rather than a free parameter, in the initial conditions. These degrees of freedom will be explored in future models. Notice that deciding whether a cloud is sub- or supercritical requires knowledge of the field strength *and* geometry.

Each run begins with a kinetic energy of $100 \rho L^3 c_s^2$, which is equivalent to an r.m.s. Mach number ($\mathcal{M} \equiv \sigma_v/c_s$) of $\sqrt{200}$. This kinetic energy is rapidly reduced by work done in bending the mean field and in compressing the isothermal fluid. It is also dissipated in shocks. The total “wave energy” (difference between the energy and that of the initial state in the absence of perturbations) dissipates on a timescale of order L/v_L , or $0.07L/c_s$. Figure 1 shows a color-coded image of the surface density in the middle of one run (**B**); here black is low density and red is high density.

In this paper we study a set of three identical experiments that differ only in the strength of the mean field. These are designated runs **A** (strong field, $\beta \equiv c_s^2/v_{A,x}^2 = 0.01$), **B** (moderate field, $\beta = 0.1$), and **C** (weak field, $\beta = 1$). Model **A** is subcritical, and models **B** and **C** are supercritical. Runs **B** and **C** undergo gravitational collapse in the sense that at some locations the density becomes very large. In run **A** the peak density rises to about $100\bar{\rho}$ after the simulation begins and then drops to only $40\bar{\rho}$ at the end of simulation. In contrast, the peak density rises almost monotonically in runs **B** and **C**, and at final stages, reaches $7.9 \times 10^4 \bar{\rho}$ (**B**) and $4.1 \times 10^4 \bar{\rho}$ (**C**). Note that this density violates the Truelove criterion³ (Truelove et al. 1997). At the end of **B**, the fraction of the mass lying at densities greater than $(1, 10, 10^2, 10^3, 10^4)\bar{\rho}$ is (75, 20, 4, 2, 1)%. At the end of **C**, the fraction of the mass lying at densities greater than $(1, 10, 10^2, 10^3, 10^4)\bar{\rho}$ is (70, 13, 3, 1.5, 0.9)%. Thus while high density, collapsed regions do develop in both supercritical runs, only a small fraction of the mass is in the highest density regions. The fraction of mass we find in collapsing regions is consistent with observations of the efficiency of star formation in giant molecular clouds as a whole (e.g., the 2% found by Myers et al. 1986).

From each of the simulations we have picked a set of “snapshots” to study intensively. They are labeled according to the run and evolution time (see Table 1). Run **B**, the moderate field ($\beta = 0.1$) run, is our “fiducial” run, i.e. the one we believe is most similar to a molecular cloud. Snapshot **B9** is our fiducial snapshot, since it is evolved enough that the velocity and magnetic field have had a chance to relax, but not so evolved that all turbulence has decayed away.

3.3. Parameters

We have to assign values to both the threshold density ρ_t and the smoothing length Δ (given in units of the grid spacing) to obtain a population of “clumps”. In addition to these two parameters there are two scaling parameters that must be chosen to give a physical scale to the simulation (there are two rather than three because gravity sets a lengthscale in the model). We fix the mean number density $n_{H_2} = 100 \text{ cm}^{-3}$ and the temperature $T = 10 \text{ K}$, corresponding to typical values found in molecular clouds. With

³ This criterion checks if the size of the Jeans length is of order a zone size or smaller. The instantaneous Jeans length is $\lambda_J^2 = \pi c_s^2 / (G\rho)$. Since c_s is constant in space and time, we can rewrite the Truelove criterion as $\rho < \frac{1}{\mathcal{T}^2} \frac{c_s^2 N^2 \pi}{GL^2}$; here N is the number of resolution elements along each axis, L is the size of the box, and \mathcal{T} , the “Truelove number” must be larger than about 4. In simulation units this becomes $\rho < 455\bar{\rho}$. Therefore we are not resolving the internal dynamics of the clump with the highest peak density.

⁴ In a real cloud, of course, radiative trapping permits regions of density lower than the critical value to contribute significantly to the observed emission, so the ^{12}CO -emitting regions in a real cloud might be somewhat larger than our defined clumps; clumps observed in optically-thinner lines like ^{13}CO or C^{18}O clumps may be closer in size to the condensations defined by our density threshold.

these scaling parameters $\bar{\rho} = n_{H_2} \mu = 3.84 \times 10^{-22} \text{ g cm}^{-3}$ for $\mu = 2.4 m_p$, $c_s = \sqrt{kT/\mu} = 0.19 \text{ km s}^{-1}$, $L = n_J c_s \sqrt{\pi / (G\bar{\rho})} = 6.45 \text{ pc}$ (since $n_J = 3$). Also the total mass $M_{\text{tot}} = \bar{\rho} L^3 = 1532 M_\odot$.

Once the scaling parameters have been chosen there is a natural choice for the threshold density ρ_t – the density corresponding to the critical density for $\text{CO}(J = 1 \rightarrow 0)$ line, $\sim 10^3 \text{ cm}^{-3}$.⁴ Since $\bar{n}_{H_2} = 100 \text{ cm}^{-3}$, $\rho_t = 10 \bar{\rho}$.

There is no equally simple way to set the smoothing parameter Δ . The purpose of smoothing the dataset before picking out the density maxima is to avoid separation of closely spaced density peaks into separate clumps; one does not want to attach too much significance to objects separated by only one grid zone. This suggests fixing $\Delta \sim 1$. The number of clumps decreases as smoothing is increased, however, so choosing Δ too large would result in the loss of most clumps and most of the information contained in the dataset. We have experimented with $\Delta = 1, 1.5$, and 2. All these give similar results. All results reported here are for $\Delta = 1.5$ unless otherwise noted. To avoid making an arbitrary choice of this kind one may alternatively consider an ensemble of clump sets defined by allowing Δ to vary from 1 to $N/2$, where N is the number of zones. This is operationally similar to the technique employed in Ostriker et al. (2001); Ostriker (2002) (and also in the analysis of large-scale cosmological structure).

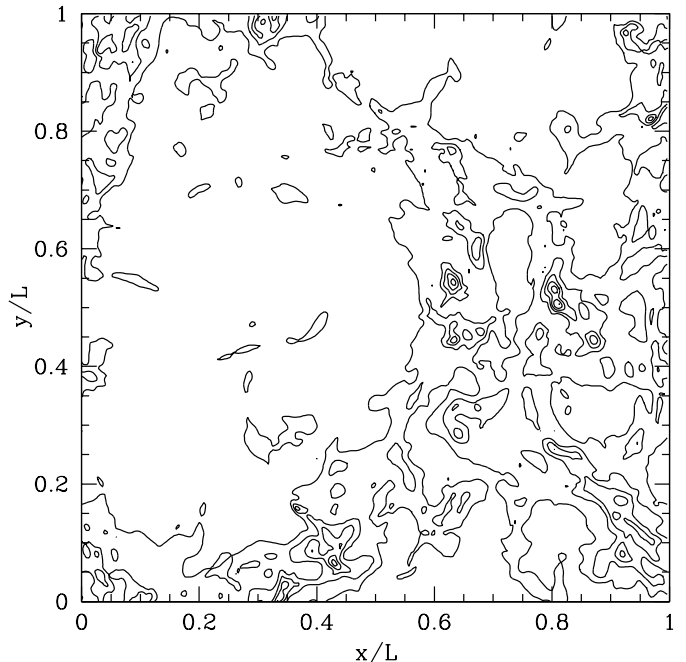


FIG. 2.— A contour plot of the surface density in snapshot **B9** from our fiducial run.

Are the clumps well resolved? To decide this issue, we define an effective radius $r_{eff}^2 \equiv \int \rho r^2 / M_{cl}$, where the in-

TABLE 1
RUNS AND RUN SNAPSHOTS

Run Name	Snapshot number	time [L/c _s]	v _{A,x} /c _s	peak density	E _{kin}	E _{δB}	t _f	resolution
A	0	0	10	1.00	100.	0.00	0.297	256 ³
	3	0.03		1.06 × 10 ²	38.4	32.7		
	7	0.07		98.6	27.7	14.6		
	19	0.19		38.2	12.2	4.00		
	29	0.29		38.5	8.56	2.26		
B	0	0	√10	1.00	100.	0.00	0.195	256 ³
	3	0.03		1.16 × 10 ²	38.5	19.7		
	4	0.04		1.30 × 10 ²	28.7	20.3		
	9	0.09		1.74 × 10 ²	11.9	13.4		
	11	0.11		3.19 × 10 ²	10.3	10.2		
	19	0.19		7.91 × 10 ⁴	7.31	4.10		
C	0	0	1	1.00	100	0.00	0.154	256 ³
	3	0.03		1.49 × 10 ²	44.1	5.15		
	5	0.05		1.34 × 10 ²	26.0	5.80		
	9	0.09		1.91 × 10 ²	12.0	5.97		
	11	0.11		2.96 × 10 ²	8.16	6.00		
	15	0.15		4.06 × 10 ⁴	4.57	5.54		

tegral is taken over the clump volume, r is measured from the clump center of mass, and M_{cl} is the clump mass. The distribution of r_{eff} depends on Δ . For $\Delta = 1.5$ the clump size distribution in snapshot **B9** (our fiducial snapshot) is such that 97% of the clumps have an effective radius $r_{eff} \geq 3$ grid zones, 78% have $r_{eff} \geq 5$ grid zones, and 15% have $r_{eff} \geq 10$ grid zones. Similar results are obtained for other snapshots. Thus most clumps are (at this stage of the evolution) well resolved.

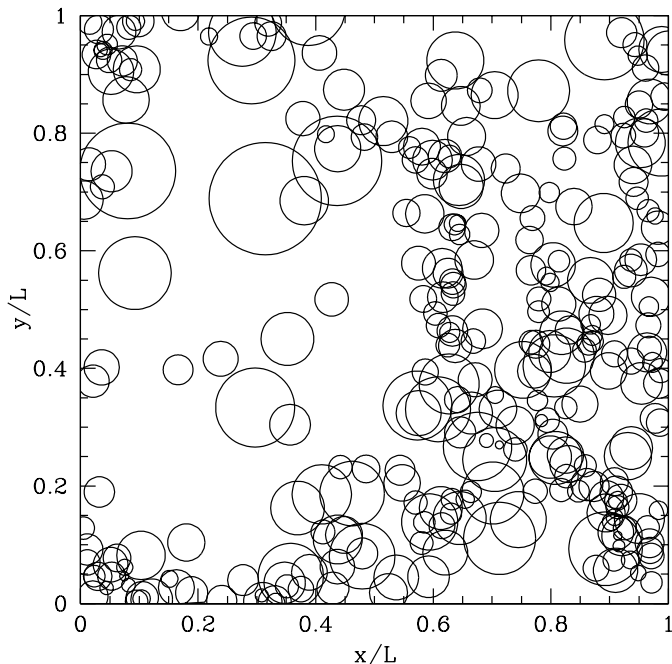


FIG. 3.— The location of 3D clumps (for definition see text) in snapshot **B9**, projected into the same plane as Figure 2. The center of each circle is at the clump center of mass, and its radius is equal to the clump effective radius.

Are the 3D clumps identified with this set of parameters at all related to 2D clumps (i.e. the clumps found by applying our clump finding algorithm to column density maps)? Figure 2 shows the column density contours for a line of sight aligned with one of the simulation box axes, and Figure 3 shows the positions of 3D clumps projected onto the same plane. The 3D clumps tend to be located in regions of large column density, but the mass and volume fractions of 3D clumps and 2D clumps differ sharply. The 3D clumps comprise 0.142 M_{tot} and 0.008 L^3 ; in projection the 3D clumps cover 39% of the cloud. The 2D clumps comprise 0.325 M_{tot} and 0.526 L^2 . The column density is thus a good tracer of the dense portions of molecular clouds, but much of the contribution to each column may come from regions with density below threshold or even from regions spatially separated from 3D clumps (see Ostriker et al. 2001).

4. CLUMP MASS SPECTRUM

The simplest property of simulated clumps that we can study is their mass spectrum. We characterize the mass spectra by four numbers: the maximum clump mass M_{max} , the minimum clump mass M_{min} , the mass corresponding to the peak of the spectrum M_{peak} (defined as the maximum of $dN/d \ln M$ for data binned in $\ln M$) and the slope of the high-mass wing, x . The slope x is determined by binning the clumps in $\ln M$ and performing a linear fit to $dN/d \ln M \propto M^{-(x-1)}$, weighted according to the square root of the number of clumps in a bin in the range $M_{peak} < M < M_{max}$. Table 2 gives a summary of the mass spectrum characteristics for each of the snapshots.

In measuring x our intent is simply to characterize the shape of the mass spectrum in a way that is similar to that used by observers, not to suggest that the underlying spectrum is a power law. Other forms of the mass spec-

trum may well provide a better fit. Also notice that the measurement of x is noisy because of the small number of clumps in the high mass wing. It can change by ± 0.3 depending on the choice of bin size and location.

The minimum clump mass M_{min} may be influenced by numerical resolution. We do not have a resolution study in hand and so we cannot quantitatively evaluate this. The minimum clump mass permitted by our clump finding algorithm is the mass in a single zone that exceeds the threshold density. This is $(10/256^3)M_{tot} = 9.1 \times 10^{-4} M_{\odot}$, which is much smaller than our typical M_{min} . This is reassuring, but because the smallest clumps typically consist of a small number of zones the reader is cautioned against placing too much weight on our measurements of M_{min} .

Consider the mass spectrum of the fiducial snapshot **B9**, which is in many respects typical (Figure 4, solid line). A total of 300 clumps were identified, accounting for 14.2% of the total mass and 0.871% of the volume. The slope of the spectrum is $x = 2.35$ (it is an accident that this is so close to the Salpeter slope for the stellar initial mass function [IMF], since different values of the smoothing parameter Δ and different binning schemes give values of x that vary by as much as ± 0.3). The maximum mass $M_{max} = 5 \times 10^{-3} M_{tot}$, the minimum mass $M_{min} = 6 \times 10^{-5} M_{tot}$, and the peak mass $M_{peak} = 3 \times 10^{-4} M_{tot}$. In physical units the peak mass is close to $0.5 M_{\odot}$, and the minimum and maximum to 0.1 and $8 M_{\odot}$, respectively. Clearly this is an interesting range of masses if clumps like these are the immediate precursors of star formation, but it is important to remember the numerical limitations of our study. In particular we do not know how these values might vary with initial conditions, Jeans number n_J , Mach number, or numerical resolution.

We expect that some clumps are transients, the result of collisions between oppositely moving streams of gas in which gravity plays no role, while others are long lived and self-gravitating. To measure the importance of gravity for each clump we define

$$\alpha \equiv \frac{E_g}{2E_k + 3E_p + E_b}, \quad (2)$$

where $E_g = (1/2) \int (\rho - \bar{\rho}) \phi d^3r$ ⁵, $E_k = (1/2) \int \rho (v - v_{cm})^2 d^3r$, v_{cm} is the clump center-of-mass velocity; $E_p = \int \rho c_s^2 d^3r$ is related to the internal energy and $E_b = \int B^2 / (8\pi) d^3r$ is the magnetic energy inside the clump; in each case the integral is taken over the clump volume. We somewhat arbitrarily label clumps as self-gravitating if $\alpha \geq 0.5$ and nonself-gravitating otherwise. Notice that our α is slightly different from the usual “virial parameter”, which is proportional to the ratio of gravitational potential energy to kinetic energy. We will analyze the kinematics of clumps by the virial theorem in greater detail in a later paper (see, e.g., Zweibel 1990; McKee & Zweibel 1992; Bertoldi & McKee 1992; Ballesteros-Paredes et al. 1999).

We show in Figure 4 the mass spectra for self-gravitating (dotted line) and nonself-gravitating (dashed line) clumps in snapshot **B9**. At this stage only 4% of the clumps (about 14% of total clump mass) are self-gravitating, and all self-gravitating clumps are in the high-mass wing of

the spectrum. The majority of the clumps are nonself-gravitating, and thus x for all clumps and for the nonself-gravitating subset are about the same.

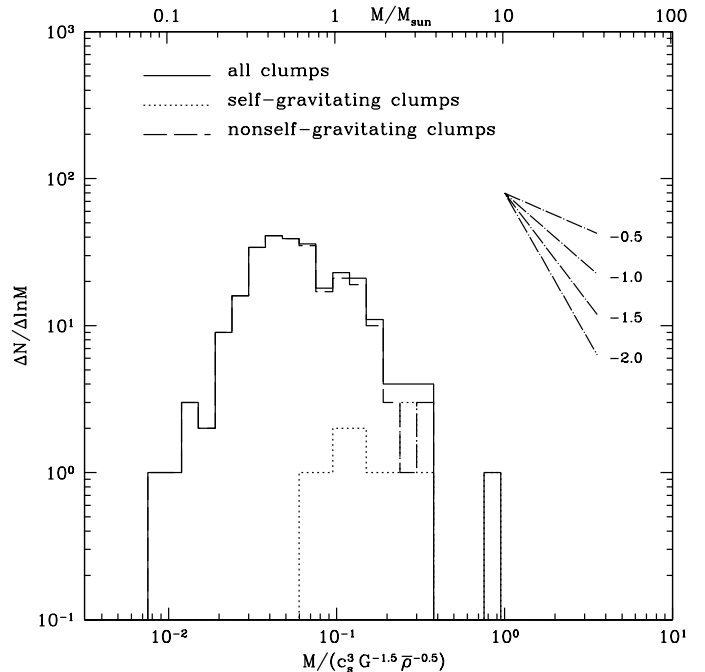


FIG. 4.— Mass spectra of self- and nonself-gravitating clumps and all clumps from snapshot **B9**. The mass unit is $c_s^3 G^{-1.5} \bar{\rho}^{-0.5} \simeq 10.2 M_{\odot}$.

How does the clump mass spectrum evolve (see, e.g., Williams & Blitz 1998)? In Figure 5 we show the mass spectra from the fiducial, earliest and last snapshots in run **B**. Several features stand out: (1) M_{max} increases with time. From the first to last snapshot M_{max} has increased about an order of magnitude. On the other hand, M_{min} remains about the same. (2) M_{peak} remains about the same. (3) The number of clumps at peak (per bin) and the total clump number decrease with time. This is a result of clump agglomeration. Notice that, although in runs **B** and **C** the total clump number decreases with time, the total mass contained in clumps increases. Evidently clumps also accrete mass from lower-density material. (4) The slope of the high-mass wing becomes “shallower”, i.e., x decreases: $x(\mathbf{B3}) = 3.15$, $x(\mathbf{B9}) = 2.35$, $x(\mathbf{B19}) = 1.98$. (5) The number of self-gravitating clumps increases, especially in the high-mass wing: in the fiducial snapshot there are only 13 self-gravitating clumps, but in the last snapshot the entire high-mass wing is comprised of such clumps (extending down to $M_{peak} \approx 0.6 M_{\odot}$).

Does the field strength influence the mass spectrum? Figure 6 shows mass spectra from snapshots **A19**, **B9**, and **C9**. We have chosen to compare these snapshots because all have similar sonic Mach numbers $\mathcal{M} \approx 5$. For the two supercritical runs (**B** and **C**) the mass spectra are similar. The subcritical run (**A**), however, is different: there are essentially no self-gravitating clumps in any of the snapshots and the mass spectrum changes in time in such a way that the number of clumps *decreases* as the evolution progresses.

⁵ This is the gravitational contribution to the total, conserved energy under periodic boundary conditions.

TABLE 2
STATISTICS OF RUN SNAPSHOTS

Snapshot no.	no. clumps	clump mass ^a	sg clump mass ^b	x^c	x_{sg}	x_{nsg}	M_{max}/M_{tot}	M_{peak}/M_{tot}	M_{min}/M_{tot}
A3	304	0.117	0	3.8	N/A	3.8	2×10^{-3}	4×10^{-4}	4×10^{-5}
A7	359	0.131	0	2.7	N/A	2.7	2×10^{-3}	3×10^{-4}	3×10^{-5}
A19	82	0.033	0	1.6	N/A	1.6	3×10^{-3}	2×10^{-4}	6×10^{-5}
A29	32	0.017	0	0.5	N/A	0.5	2×10^{-3}	4×10^{-4}	7×10^{-5}
B3	285	0.083	0	3.2	N/A	3.2	2×10^{-3}	4×10^{-4}	2×10^{-5}
B4	327	0.096	0.009	2.7	N/A	2.7	1×10^{-3}	2×10^{-4}	3×10^{-5}
B9	300	0.142	0.138	2.4	N/A	2.5	5×10^{-3}	3×10^{-4}	6×10^{-5}
B11	340	0.163	0.277	2.3	2.0	2.5	6×10^{-3}	3×10^{-4}	4×10^{-5}
B19	196	0.207	0.844	2.0	1.9	1.9	1×10^{-2}	4×10^{-4}	7×10^{-5}
C3	303	0.113	0.002	3.0	N/A	3.0	2×10^{-3}	4×10^{-4}	5×10^{-5}
C5	298	0.101	0.127	2.5	N/A	2.5	2×10^{-3}	2×10^{-4}	4×10^{-5}
C9	233	0.110	0.377	2.2	1.6	2.1	4×10^{-3}	4×10^{-4}	6×10^{-5}
C11	214	0.129	0.526	2.3	1.8	2.0	7×10^{-3}	2×10^{-4}	6×10^{-5}
C15	182	0.141	0.832	1.6	1.2	2.1	2×10^{-2}	2×10^{-4}	3×10^{-5}

^aMass fraction in clumps.

^bMass fraction in self-gravitating clumps.

^cThe uncertainty in the mass spectrum slope x is $\sim \pm 0.3$

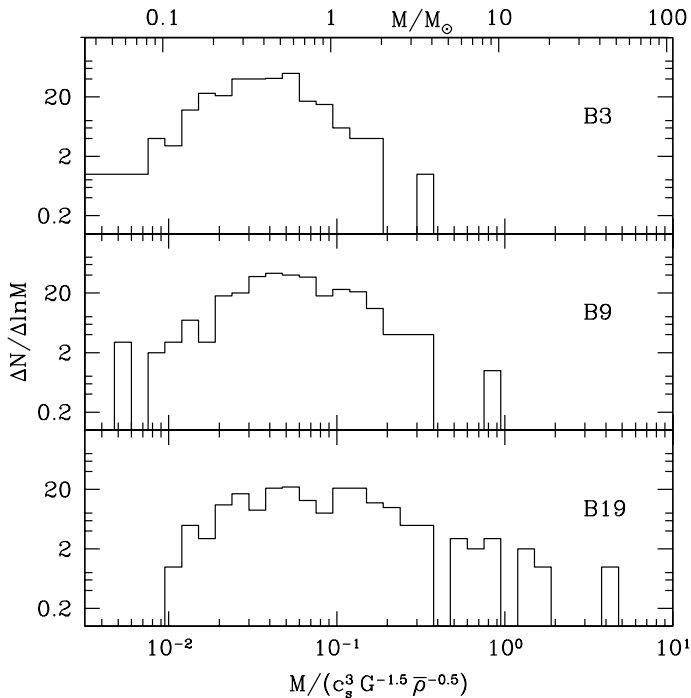


FIG. 5.— The evolution of the clump mass spectrum in the fiducial run **B**.

Finally, do projection effects change the mass spectrum? We have examined the mass spectrum of clumps in column density maps made from our simulations. We use precisely the same clump definition for the column density maps as in our 3D density fields, except that no smoothing is applied ($\Delta = 0$, since the transformation to column density is effectively a smoothing operation) and the threshold column density is set to be 1.1 times the mean column density. We refer to the result-

ing clumps as “2D clumps”. We find that (1) masses of 2D clumps are larger than the 3D clumps (by about an order of magnitude) and therefore, M_{max} and M_p are both greater than those in 3D spectra. (2) The slopes are generally slightly steeper than the 3D ones and have a weak tendency to become shallower in time. For example, $x(\mathbf{B3}, 2D) = 3.26$, $x(\mathbf{B9}, 2D) = 2.49$, $x(\mathbf{B19}, 2D) = 2.50$. The 2D and 3D mass spectra for snapshot **B9** are compared in Figure 7.

5. CLUMP SHAPES

Clump shapes may be an indicator of the dynamical processes that govern clump internal dynamics. For example, early models of magnetized, self-gravitating clouds (e.g. Mouschovias 1976) have oblate spheroidal isodensity contours that are flattened in a plane perpendicular to the mean magnetic field. Observers have looked for evidence of such oblate structures in molecular line maps of clouds.

Myers et al. (1991) (see also David & Verschueren 1987; Fleck 1992; Curry & Stahler 2001) measured the projected axis ratios (r) of 16 dense cores in dark clouds and found that $\langle r \rangle = 0.5 - 0.6$. They modeled ensembles of identical spheroidal cores, either all prolate or all oblate, assuming that their orientation in space is isotropic. Their results showed that the prolate ensemble can account for $\langle r \rangle$ with reasonable intrinsic axis ratio, while it requires *extremely* flattened oblate cores to produce same projected axis ratios. This suggests that prolate objects are preferred, contrary to the prediction of static, magnetized models.

Ryden (1996) obtained a tighter constraint on the shapes of clouds by studying the full distribution of apparent axis ratios $f(r)$. For several samples of dense interstellar clouds, including Bok globules, dense cores, and clumps, she mapped the estimated distribution $f(r)$ into a distribution of intrinsic axis ratios under the hypothesis

that the clouds were oblate or prolate spheroids. She found that for most of her cloud samples the data were inconsistent, or at best marginally consistent, with the hypothesis that clouds are oblate spheroids because of a lack of almost circular ($r \sim 1$) objects. The samples were consistent with the hypothesis that the clouds were prolate spheroids.

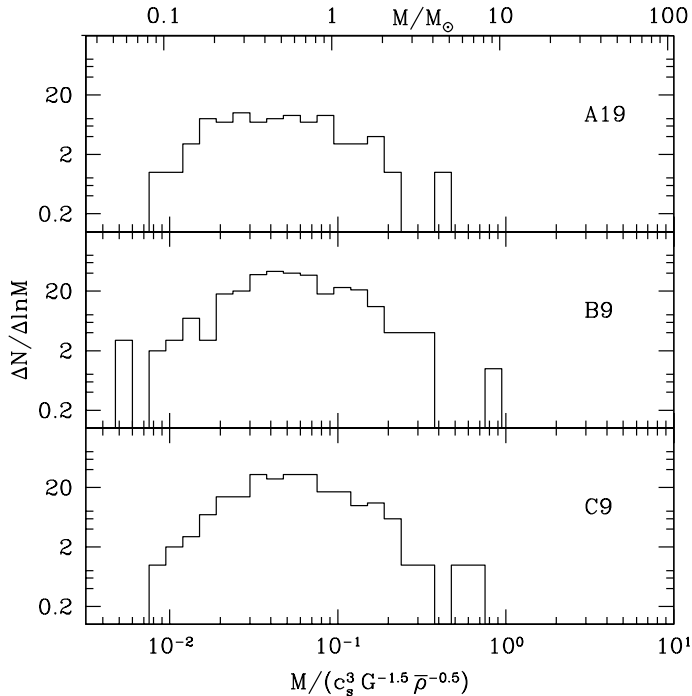


FIG. 6.— The dependence of clump mass spectrum on initial magnetic field strength in snapshots from each of the three runs. The snapshots are selected so that the turbulent sonic Mach number is nearly constant.

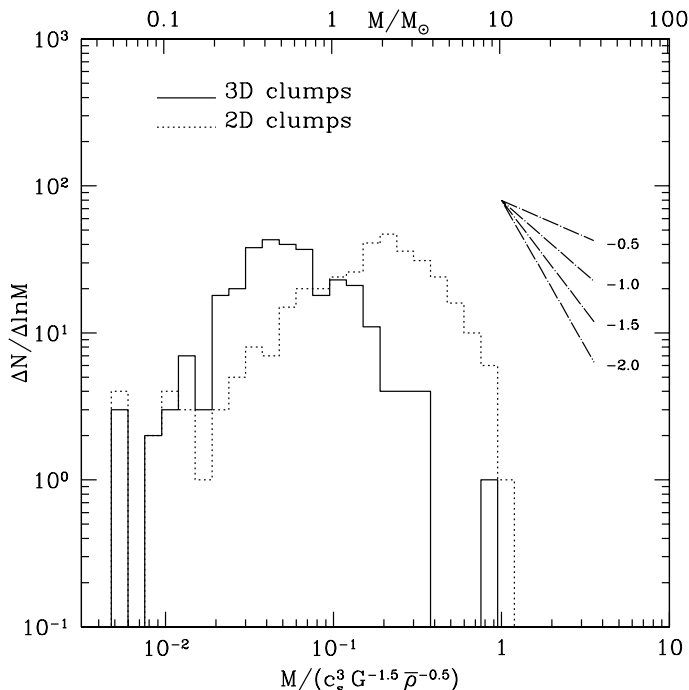


FIG. 7.— Comparison of clump mass spectra for clumps identified in three dimensions (3D clumps) with those identified from column density maps in B9. The differences arise in part from the overlapping of 3D clumps in projection.

We have performed a similar analysis of a subset of the catalog of clumps in the M17 SW cloud developed by Stutzki & Güsten (1990) using their GAUSSCLUMPS clump finder. We have restricted attention to those clumps with minor axis FWHM larger than $20''$ to minimize the effects of rounding by the $13''$ FWHM beam, and we have subtracted the beam size in quadrature from the axis lengths given in the paper. Notice that GAUSSCLUMPS uses a slightly different definition of clumps and principal axis lengths from ours. Given this sample of clump principal axis lengths, it is possible to construct an estimate for the continuous distribution $f(r)$ via the nonparametric kernel estimator used by Ryden (we use a kernel width $h = 0.08$, on a sample of 41 clumps). The result is shown in Figure 8 as a bold dashed line (Figure 9 shows the same result applied to “2D clumps”; see below). The light dashed lines show the uncertainties in $f(r)$ estimated via a bootstrap resampling technique. The mean axis ratio $\langle r \rangle = 0.61$. Recall that $\langle r \rangle > 0.5$ for oblate spheroids.

As for elliptical galaxies one can only infer the intrinsic shape of a population of *spheroidal* clouds from a set of axis ratios. If the underlying population is triaxial, no such inference is possible, since a mapping from a distribution with one axis ratios to that with two axis ratios is degenerate.

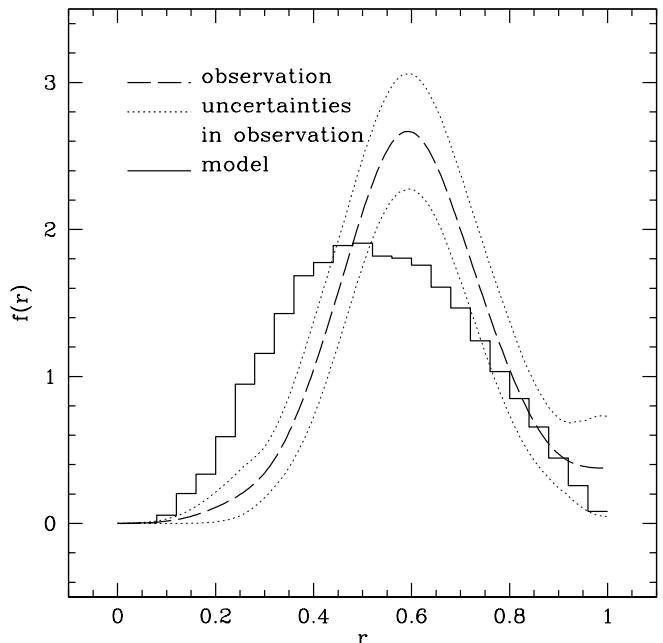


FIG. 8.— The distribution of apparent axis ratios of 3D clumps (histogram) in our model and the distribution of apparent axis ratios in Stutzki & Güsten’s (1990) catalog of clumps from M17SW derived using Ryden’s (1996) method.

5.1. Clump Shape Definition

We characterize clump shapes using the eigenvalues of the moment of inertia tensor:

$$I_{ij} \equiv \int d^3\mathbf{r} \rho x_i x_j. \quad (3)$$

Here \mathbf{x} is measured relative to the clump center of mass. The eigenvalues are $Ma^2 \geq Mb^2 \geq Mc^2$, where M is

the clump’s mass and a, b, c are the principal axis lengths. The corresponding eigenvectors $\mathbf{e}_a, \mathbf{e}_b, \mathbf{e}_c$ are the principal axes. The intrinsic shape can be characterized via the axis ratios $\tilde{\beta} \equiv b/a$ and $\tilde{\gamma} \equiv c/a$ (note that $\tilde{\beta}$ differs from the plasma β).

One advantage of using the moment of inertia tensor to measure clump shape is that it can be related to observations, which are done in two dimensions on the sky. The projection of the moment of inertia tensor is

$$P_{ij} \equiv \int d^2\mathbf{r} \Sigma X_i X_j. \quad (4)$$

Here $X_{1,2}$ are Cartesian coordinates on the plane of the sky and Σ is the surface density or anything proportional to the surface density, such as total flux in an optically thin line that traces the density. P has eigenvalues $Mp^2 \geq Mq^2$. The apparent shape is characterized by the apparent axis ratio $r \equiv q/p$. This is what can be measured by an observer from column density maps of an isolated clump.

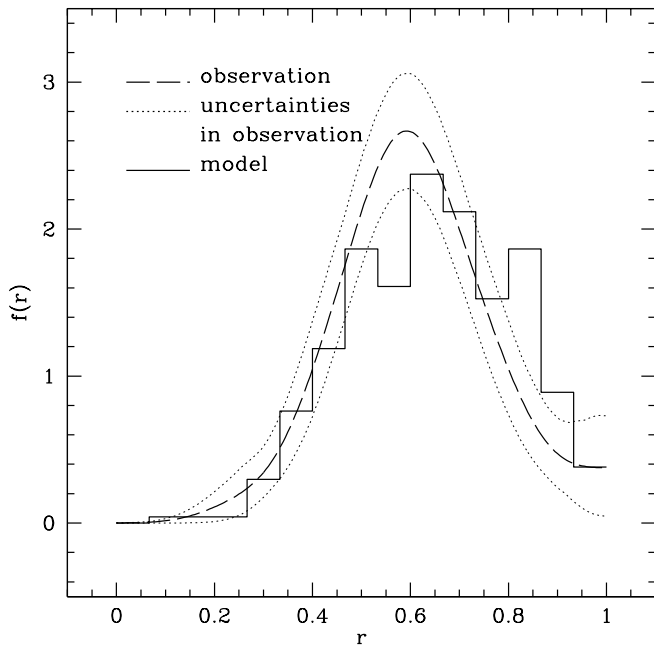


FIG. 9.— The distribution of axis ratios for 2D clumps (histogram) together with the M17SW clump distribution from Stutzki & Güsten’s (1990), as in Figure 8.

The apparent shape can be calculated from the eigenvalues a, b, c of the moment of inertia tensor without actually projecting the clump pixel by pixel (this is computationally useful). Let θ be the angle between \mathbf{e}_c and line-of-sight, and ϕ be the angle between \mathbf{e}_a and \mathbf{x} , which points along the intersection of the $\mathbf{e}_a, \mathbf{e}_b$ plane with the plane of the sky. Then the apparent axis ratio is

$$r = \left(\frac{P_{xx} + P_{yy} - \sqrt{P_{xx}^2 + 4P_{xy}^2 - 2P_{xx}P_{yy} + P_{yy}^2}}{P_{xx} + P_{yy} + \sqrt{P_{xx}^2 + 4P_{xy}^2 - 2P_{xx}P_{yy} + P_{yy}^2}} \right)^{1/2} \quad (5)$$

where $P_{xx} = a^2 \sin^2 \theta + b^2 \cos^2 \theta \sin^2 \phi + c^2 \cos^2 \theta \cos^2 \phi$, $P_{xy} = (b^2 - c^2) \cos \theta \cos \phi \sin \phi$, $P_{yy} = b^2 \cos^2 \phi + c^2 \sin^2 \phi$.

Finally, some terminology: the term “projected clump” as used here refers to an object found by our clumpfinder in three spatial dimensions (a 3D clump) and then projected as if it were completely isolated onto the sky. The term “2D clump” refers to an object found by our clumpfinder in two spatial dimensions, after the entire density field has been projected on the sky. Were all 3D clumps well separated these procedures would yield identical results. However 3D clumps overlap in projection and therefore the populations differ.

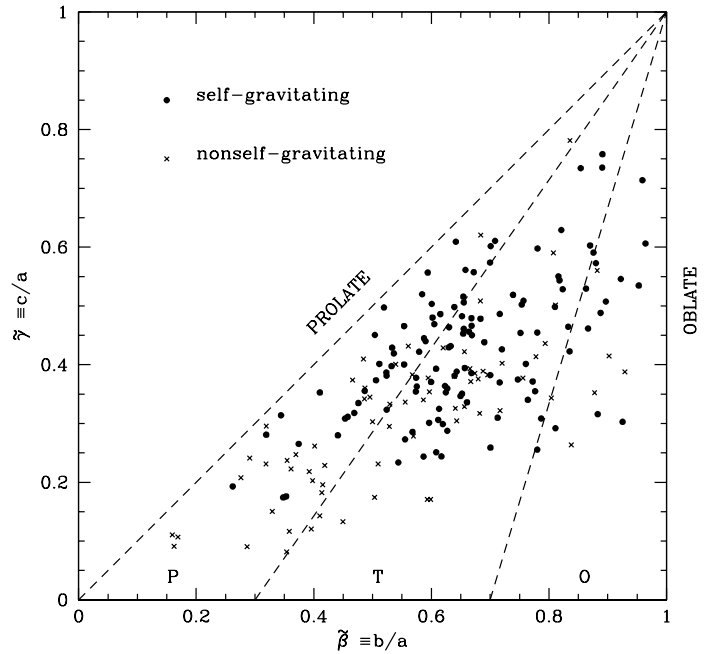


FIG. 10.— The distribution of 3D clump axis ratios in B9. Clumps lying on the diagonal are prolate ($b/a = c/a < 1$); clumps lying along the right hand boundary of the plot are oblate ($a/b = 1$; $c < 1$). We have divided the diagram into three regions: prolate (within the triangle marked P); triaxial (within the triangle marked T); and oblate (within the triangle marked O). The precise boundaries of these regions are arbitrary.

5.2. 3D Axis Ratios

Figure 10 shows the distribution of true axis ratios in B9. The self-gravitating clumps are denoted as solid dots, while nonself-gravitating clumps are crosses. The clumps are truly triaxial in the sense that they do not cluster around the prolate or oblate axes. As a convenience, we divide the $\tilde{\beta} - \tilde{\gamma}$ plane into three parts: a “prolate” part (which lies above the line connecting $(\tilde{\beta}, \tilde{\gamma}) = (1.0, 1.0)$ and $(0.33, 0.0)$), an “oblate” group (which lies below the line connecting $(\tilde{\beta}, \tilde{\gamma}) = (1.0, 1.0)$ and $(0.67, 0.0)$), and a “triaxial” group (everything else). Of the 300 clumps, 41% are prolate, 47% are triaxial, and only 12% are oblate. Although the relative clump numbers vary from snapshot to snapshot, in general the prolate and triaxial groups comprise about 90% of the clumps. A purely spheroidal (oblate or prolate) model for the intrinsic clump shape distribution is not viable.

The prolate, oblate, and triaxial fraction for each snapshot are listed in Table 3. The only trend worth remarking on is the growth in prolate clumps with time in run A. As we shall see below, these objects have a weak tendency

to line up so that the long axis is perpendicular to the magnetic field.

The broad distribution of clump shapes in the $\tilde{\beta} - \tilde{\gamma}$ plane is likely telling us that clumps have complicated internal dynamics—they are turbulent—and are not well described by highly symmetric equilibrium models. The self-gravitating clumps, however, are slightly “rounder” than nonself-gravitating ones; they tend to lie closer to the point $(\tilde{\beta}, \tilde{\gamma}) = (1.0, 1.0)$ than their nonself-gravitating counterparts (this is not a resolution effect, as self-gravitating clumps tend to be larger and hence better resolved than nonself-gravitating clumps).

5.3. Apparent Axis Ratio

The procedure for obtaining the apparent axis ratio of a 3D clump was described in §5.1. If we apply this procedure to every clump and average over many viewing angles, we can obtain a mean, or expected distribution for $f(r)$. Figure 8 (solid line) shows the distribution of the apparent axis ratios obtained from **B9**, as well as the result from M17SW (Stutzki & Güsten 1990).

Crudely speaking, the two distributions are consistent in the sense that both show a characteristic absence of nearly round objects. It is this absence that most strongly rules out a parent population of oblate spheroids (Ryden 1996). The $f(r)$ changes with time in the sense that the mean apparent axis ratio increases. In fact, $f(r)$ for snapshots **B11** and **B19** lies within the error bounds permitted by the observations. A similar increase in the mean apparent axis ratio with time is seen in run **C** (the clumps become rounder with time), but not run **A**.

Our discussion up to now has concerned apparent axis ratios of individual clumps. Clumps exhibit considerable overlap (“confusion”), however, so the distribution of axis ratios of apparent (2D) clumps may be different from the distribution of apparent axis ratios of real (3D) clumps seen in projection. Figure 9 shows a comparison between the former (2D clumps obtained from a single line of sight projection) and the M17 observations. Broadly speaking, they are consistent with each other and the 2D clumps also show the absence of round clumps.

6. CLUMP ORIENTATION

Steady-state theoretical models of magnetically supported clouds suggest that clouds should be flattened perpendicular to the magnetic field (e.g., Mouschovias 1976; Tomisaka et al. 1988a,b; Baureis et al. 1989; Lizano & Shu 1989; Galli & Shu 1993; Fiedler & Mouschovias 1993; Li & Shu 1996) or, in the language of this paper, that the clump minor axis should be nearly parallel to the local field. Observations by Goodman et al. (1990) (also Goodman et al. 1992) suggest, however, that cloud minor axes are not correlated with the local field direction. Recent observations showing alignment (Matthews & Wilson 2000) are for a small number of clumps in individual clouds and probably do not indicate a statistically significant alignment⁶. Here we examine correlations between the clump principal axes and the *density-weighted* mean field within clumps, as well as the mean global fields, $\langle \mathbf{B} \rangle$.

⁶ Assessing the statistical significance of alignments is complicated by the fact that both magnetic fields and clump orientations are spatially correlated.

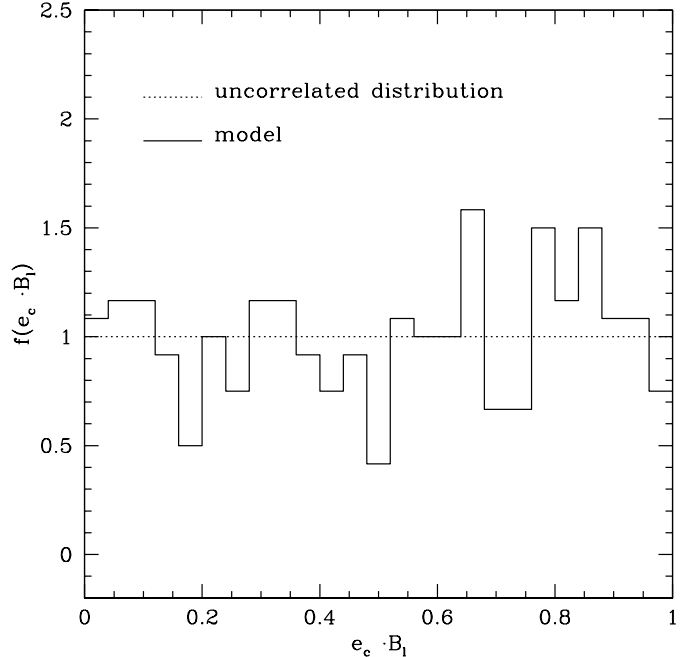


FIG. 11.— The distribution of angles between the shortest body axis and the density weighted mean magnetic field in the clump in **B9**. The dashed line shows the distribution expected if both vectors are chosen randomly.

Figure 11 shows the distribution of the dot product of the clump short axis unit vector (\mathbf{e}_c) and the unit vector associated with the density weighted mean magnetic field in the clump (\mathbf{b}_l) in snapshot **B9**. The dashed line shows the distribution expected if both vectors are chosen at random. Evidently there is no strong correlation between the mean local field and the clump minor axis.

Figure 12 shows a similar plot for 3D clumps in projection, also for **B9**. The distribution is obtained as follows: for a fixed viewing angle, we use the same procedure described in §5 to obtain the principal axes of the projected clump, as well as the density-weighted magnetic field vector within each clump. Averaging over 10^4 viewing angles gives the distribution. Again there is no strong correlation between the local mean field and the clump minor axis.

A more complete description of alignment statistics is given in Table 3. There we list, for each of the snapshots, the fractional alignment of clump axes and the global and local mean fields. The quantity $\mathcal{L.A.}$, for example, is the fraction of all clumps with $|\mathbf{e}_a \cdot \mathbf{b}_l| > 0.86$, i.e. the fraction of all clumps with major axis closer than 30° to the local mean field. Similarly, $\mathcal{L.B.}$ is the fraction of all clumps with intermediate axis closer than 30° to the local mean field, etc.

Table 3 also describes the alignment of clump axes with the global volume mean magnetic field with unit vector \mathbf{b}_g . The quantity $\mathcal{G.A.}$ is the fraction of all clumps with $|\mathbf{e}_a \cdot \mathbf{b}_g| > 0.86$. The only significant global alignment is in the late stages of the strong field run, when the short axis has a weak tendency to line up with the global mean field.

TABLE 3
SHAPE AND MAGNETIC FIELD ALIGNMENT IN CLUMP SNAPSHOTS

Snapshot no.	clump shape \mathcal{P}^a \mathcal{T}^a \mathcal{O}^a			local alignment			global alignment			proj. align.	
				long $\mathcal{L}.\mathcal{A}.$ ^b	int. $\mathcal{L}.\mathcal{B}.$ ^b	short $\mathcal{L}.\mathcal{C}.$ ^b	long $\mathcal{G}.\mathcal{A}.$ ^c	int. $\mathcal{G}.\mathcal{B}.$ ^c	short $\mathcal{G}.\mathcal{C}.$ ^c	long $\mathcal{P}.\mathcal{A}.$ ^d	short $\mathcal{P}.\mathcal{B}.$ ^d
A3	0.43	0.42	0.15	0.06	0.09	0.15	0.14	0.15	0.13	0.27	0.38
A7	0.48	0.41	0.11	0.11	0.13	0.14	0.13	0.12	0.13	0.30	0.36
A19	0.50	0.39	0.11	0.07	0.13	0.22	0.07	0.12	0.18	0.26	0.41
A29	0.56	0.31	0.13	0.00	0.13	0.25	0.00	0.09	0.25	0.21	0.44
B3	0.47	0.46	0.07	0.14	0.16	0.13	0.12	0.12	0.16	0.35	0.32
B4	0.46	0.42	0.12	0.14	0.14	0.12	0.14	0.11	0.16	0.34	0.32
B9	0.41	0.47	0.12	0.14	0.12	0.14	0.10	0.15	0.15	0.33	0.33
B11	0.48	0.42	0.10	0.11	0.10	0.16	0.14	0.10	0.12	0.30	0.36
B19	0.41	0.47	0.12	0.10	0.12	0.20	0.14	0.12	0.15	0.29	0.39
C3	0.42	0.44	0.14	0.21	0.17	0.04	0.10	0.12	0.11	0.44	0.24
C5	0.42	0.46	0.12	0.17	0.15	0.09	0.13	0.10	0.10	0.37	0.30
C9	0.48	0.40	0.12	0.13	0.15	0.10	0.12	0.09	0.18	0.36	0.31
C11	0.42	0.45	0.13	0.14	0.14	0.12	0.10	0.13	0.14	0.36	0.31
C15	0.53	0.37	0.10	0.13	0.14	0.10	0.10	0.14	0.18	0.34	0.31

^aFraction of prolate (\mathcal{P}), triaxial (\mathcal{T}) and oblate (\mathcal{O}) clumps.

^bFraction of clumps whose density-weighted mean magnetic field is within 30 deg of the clump major axis ($\mathcal{L}.\mathcal{A}.$), within 30 deg of the intermediate axis ($\mathcal{L}.\mathcal{B}.$), or within 30 deg of the major axis ($\mathcal{L}.\mathcal{C}.$).

^cFraction of clumps for which the global mean magnetic field is within 30 deg of the clump minor axis ($\mathcal{G}.\mathcal{A}.$), etc..

^dFraction of clumps for which the projected density weighted mean magnetic field is within 30 deg of the projected minor axis ($\mathcal{P}.\mathcal{A}.$), etc..

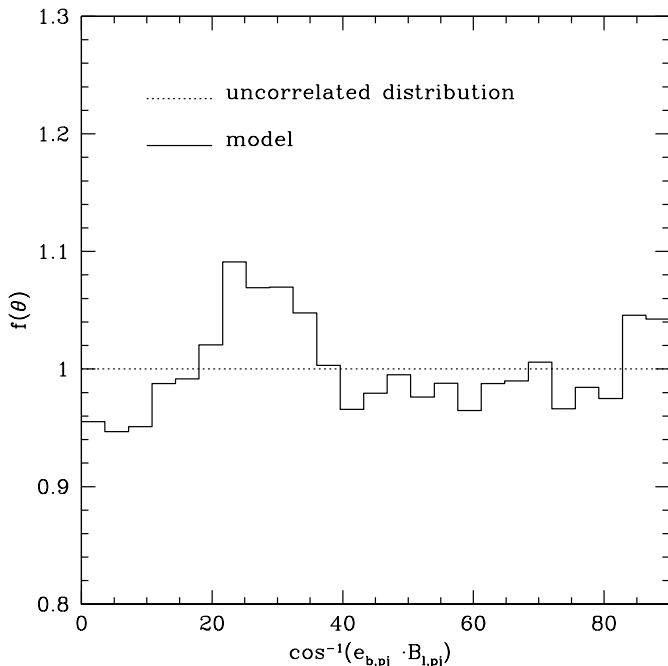


FIG. 12.— The distribution of angles between the projected shortest body axis and the projected density weighted mean magnetic field in **B9**. The dashed line shows the distribution expected if both vectors are chosen randomly.

Notice that if clump magnetic fields are randomly oriented with respect to the clump principal axes, *and* if the orientation of each clump is independent, we expect $\mathcal{L}.\mathcal{A}. = 0.14 \pm 0.52/\sqrt{N}$ at the 87% confidence level, where

N is the number of clumps (and similarly for $\mathcal{L}.\mathcal{B}.$, $\mathcal{L}.\mathcal{C}.$, etc.). This naïve estimate for the dispersion in alignments is not accurate because clump orientations are probably spatially correlated (i.e. not independent). For example consider run **C**, whose weak initial field makes any global alignments physically implausible. Nevertheless, **C** exhibits global alignments that are “statistically significant” according to our naïve estimate.

The only significant and physically plausible alignments occur in run **A**, where we find that the minor axis tends to be weakly aligned with the field. The longest axis also tends to be anti-aligned with the field. This is similar to what might be expected from an equilibrium model, except that the clump shapes tend to be dominantly prolate or triaxial rather than oblate.

Table 3 also describes the alignment of projected mean field vectors with the principal axes of the projected moment of inertia tensor. These alignments are given in the final two columns ($\mathcal{P}.\mathcal{A}.$ and $\mathcal{P}.\mathcal{B}.$, which are the fraction of clumps with projected field less than 30° from the projected clump major and minor axes, respectively). For randomly oriented clumps we expect $\mathcal{P}.\mathcal{A}. = \mathcal{P}.\mathcal{B}. = 0.33$. The projected alignments are sensitive to viewing angle, so the values shown have been averaged over 10^4 uniformly distributed viewing angles. The only plausible alignments are in run **A**; other snapshots show at best marginally significant alignments. To sum up, our numerical models suggest that projected alignments are weak and not a useful diagnostic of field strength.

Clump principal axis alignments, like the mass spectrum, are sensitive to the smoothing parameter Δ . For example, if $\Delta = 0$ we see an implausible set of alignments

in run **C**. Presumably this is because we are studying alignments near the grid scale. This is one of the motivations for introducing a finite Δ .

7. ROTATION

Observations suggest that rotation is not important in supporting clumps against gravitational collapse since rotational energy is small compared to the gravitational potential energy (e.g. Goodman et al. 1993). However, once collapse takes place, angular momentum may play an important role in determining the characteristics of the system to be formed, e.g., the size of circumstellar disks, or the separation of the stars in a multiple star system.

Clumps or cores are observed to have greater specific angular momentum j than binary or multiple star systems. Consider a binary with masses of $1 M_{\odot}$ for both members and a period of 100 years. The specific angular momentum of this system is $j_{bin} = 1.16 \times 10^{20} \text{ cm}^2 \text{ s}^{-1}$. This is typical for young binary T Tauri stars (e.g. Simon et al. 1995). For single protostars and the envelope, Ohashi et al. (1997) obtained $j \sim 10^{20} \text{ cm}^2 \text{ s}^{-1}$ for two IRAS sources (for circumstellar disks, see, e.g. Beckwith et al. 1990). As for dense cores, the results given by Goodman et al. (1993) range from 6×10^{20} to $4 \times 10^{22} \text{ cm}^2 \text{ s}^{-1}$.

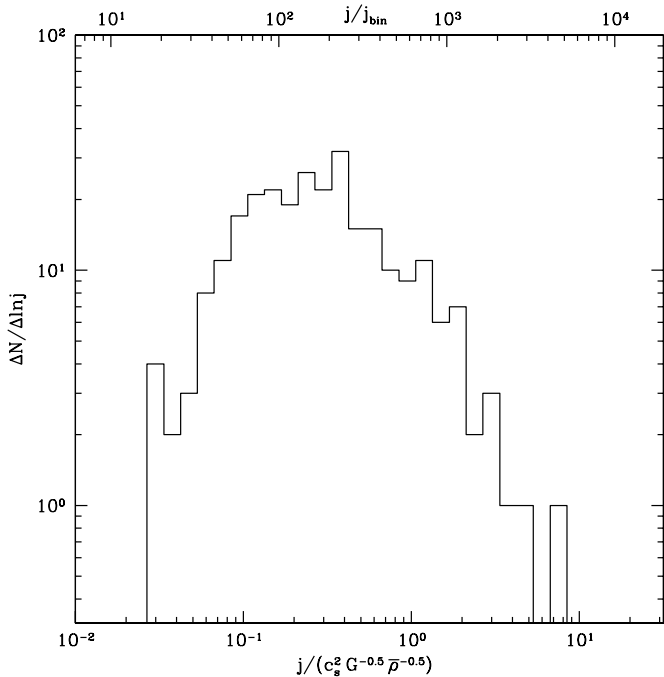


FIG. 13.— Distribution of specific clump spin angular momentum in **B9**. The normalization is to $c_s^2 G^{-0.5} \bar{\rho}^{-0.5} \equiv j_{tot}/(n_J \pi^{0.5})$, where $j_{tot} \equiv 3.8 \times 10^{23} \text{ cm}^2 \text{ s}^{-1} = 3280 j_{bin}$ and $j_{bin} \approx 10^{20} \text{ cm}^2 \text{ s}^{-1}$ is a reference angular momentum for a pair of $1 M_{\odot}$ stars in circular orbits at 100 AU.

We have examined the specific angular momenta of the simulated clumps, and find that the values are greater than j_{bin} . In Figure 13 we show the distribution of specific angular momenta of clumps in **B9**. Clump specific angular momenta span about 2 – 3 decades, e.g., from $10 j_{bin}$ to $\sim 6 \times 10^3 j_{bin}$, the peak is at $2.5 \times 10^2 j_{bin}$; the range of the distribution decreases with time in **B** and **C** snapshots (we cannot say much about run **A** because there are not many clumps in later snapshots). There is no clear trend

in clump specific angular momentum with mass.

Our distribution of specific angular momenta may be compared to those found by Burkert & Bodenheimer (2000) (hereafter BB), who studied clump models in which the internal velocities are drawn from a Gaussian random field at a spatial scale $\sim 0.1 \text{ pc}$; their power spectrum ($v^2 \propto k^{-4}$) was normalized to match the typical velocity dispersion in the Goodman et al. (1998) sample of cores. Their distribution peaks at $\sim 2 \times 10^{21} \text{ cm}^2 \text{ s}^{-1}$, while ours peaks at $4 \times 10^{22} \text{ cm}^2 \text{ s}^{-1}$. This difference is attributable to the following factors. First, our sample contains both nonself-gravitating and self-gravitating clumps, while BB’s clumps are scaled to match self-gravitating clumps. Second, the self-gravitating clumps in our sample are more massive (by a factor of about 4) than BB’s using our standard scaling. Third, the self-gravitating clumps have lower mean specific angular momentum (by about 40%) than the nonself-gravitating clumps. Fourth, while BB chose a Gaussian clump density profile, our clumps have substantial envelopes that can make a significant contribution to clump angular momentum. We conclude that the difference is not significant.

8. SUMMARY

The main results of this paper are:

1. Clumps are triaxial. Clumps that are “prolate” or “triaxial” (in the sense defined in §5) make up 90% of the clump population. Clumps that are “oblate” make up only 10% of the clump population. The distribution of clump shapes implies a distribution of apparent axis ratios that is consistent with observations. We do not see any signs of the sort of oblate equilibria that have been the focus of earlier studies of magnetized clouds emerging in our simulations. But we have not considered the most general possible set of initial states (we assume the mass-to-flux ratio is uniform), nor have we included the effects of ambipolar diffusion.

The possibility of triaxial cloud cores has also been explored by Basu (2000); Jones et al. (2001); Jones & Basu (2002). Basu (2000), however, suggested that the short axis should be aligned with the magnetic field. This is not seen in our numerical models. The absence of magnetically supported equilibria in self-gravitating, turbulent MHD models has also been noted by several other workers in the field, perhaps most forcefully by Padoan et al. (2000). The emergence of such equilibria in supersonic, self-gravitating turbulence cannot yet be ruled out, however, because the effects of ambipolar diffusion, varying mass to flux ratios, and varying initial conditions have not yet been studied.

2. Clump principal axes are not strongly aligned with the magnetic field, either locally or globally. We would not expect to see such alignments in observations, nor are they currently observed. The effect of magnetic fields on cloud structure has been considered earlier by Ballesteros-Paredes & Mac Low (2002). They found that only strong fields produce an observable effect on the density structure based on a qualitative analysis. A similar result was seen at late stages of self-gravitating evolution in the strong-field models of Ostriker et al. (1999).

3. The simulated clump mass spectrum has a characteristic mass of $\sim 0.5 M_{\odot}$ (for an assumed mean cloud density

and temperature). While this result is suggestive, it depends on some of the choices made in setting up our simulations, including numerical resolution. It is possible that the characteristic mass scales with the total cloud mass or with the sonic Mach number or density of the initial conditions. These scalings have not yet been explored. The high-mass wing of the clump mass spectrum has a slope that is crudely consistent with the Salpeter law, although other, non-power-law forms for the mass spectrum may well be consistent with our data.

Other numerical work on the clump mass spectrum by Padoan et al. (2000); Klessen (2001); Klessen & Burkert (2001); Padoan & Nordlund (2002); Ballesteros-Paredes & Mac Low (2002) is generally consistent with our results. These models include similar physics to ours, although some models lack selfgravity (Ballesteros-Paredes & Mac Low 2002), while others lack magnetic fields (Klessen 2001; Klessen & Burkert 2001).

The simulations of Padoan et al. (2000) are the most similar to those analyzed here. Differences in Padoan et al.’s analytical methods limit the possibility of detailed comparisons, however: their definition of a self-gravitating clump does not include turbulent kinetic energy; the mass spectra presented are composites of two models with gas temperatures that differ by a factor of three; their definition of a clump depends on contrast of local peaks rather than a density threshold. Nevertheless, the results of the two analyses for the position of the peak of the mass spectrum, as well as for the slope of the high-mass end, are broadly consistent.

Klessen (2001) and Klessen & Burkert (2001) use a completely different numerical method (smoothed particle hydrodynamics) and include selfgravity but not magnetic fields. In addition, they allow dense regions to turn into “sink” particles. This allows them to continue the evolution much further in time than is possible in our calculations. The trends we find of an increasingly flat high-end spectrum, and a larger proportion of mass in bound objects, are clearly evident in their distributions at sequential evolutionary stages. Their clump mass spectra are again crudely consistent with ours; minor differences in mass scale and shape may arise due to differences in initial conditions or input parameters (number of Jeans masses). We cannot evaluate this without a direct attempt to reproduce their models.

Recently, Padoan & Nordlund (2000) (see also Padoan & Nordlund 2002) have proposed that the clump mass spectrum, and consequently the mass function of collapsing cores, may be predicted solely from three macroscopic quantities averaged over the entire cloud: density, temperature, and velocity dispersion. Although this theory is attractive in many ways, the stationary turbulent state adopted for the Padoan & Nordlund (2000) may not be a good approximation for real star forming regions. Clouds are transient structures, and a cloud may have developed its current mean density, temperature, and velocity dispersion in many ways. Our analysis of purely decaying models shows that some aspects of the mass spectrum are invariant in time (e.g. M_{peak}) even as the Mach number decreases, while other aspects of the mass spectrum (the fraction of self-gravitating clumps) increase secularly with time. Both of these results suggest that a cloud retains a

memory of its dynamical history that may be important for establishing the stellar IMF.

4. Clump specific angular momenta are an order of magnitude larger than in a “typical” binary system. It is interesting that our simulations give clump angular momenta that are so close to the angular momenta of binary systems. This suggests that we are close to resolving the lengthscale where the angular momentum of binaries is determined (since $\Delta v_\lambda \sim \lambda^{1/2}$ in molecular clouds and in supersonic turbulence generally, the specific angular momentum $j \sim \Delta v_\lambda \lambda \sim \lambda^{3/2}$, so $\lambda \sim j^{2/3}$). Future higher resolution numerical models, perhaps with an adaptive mesh, will resolve this scale and may be capable of directly simulating binary formation.

Our results all depend on how the clumps are defined. Because fragmentation during gravitational collapse may decide the final stellar mass function, characterizing the hierarchy of clumpy structure and understanding its consequences may be very important. Mass functions are steeper when clumps-within-clumps are counted rather than discounted (see e.g. Ostriker 2002); whether gravity eventually selects the larger or smaller scale of a nested structure depends on the details of the collapse. More general tools (e.g. wavelet methods) for analyzing the density field will be valuable in characterizing this hierarchical structure. Future analyses should also focus on direct analogues of observable clumps (e.g. simulated clumps in position-position-velocity space for common molecular tracers), although self-consistent treatments of thermodynamics, radiative transfer, and molecular chemistry may ultimately be necessary for realistic source functions.

This work was supported by NASA grants NAGW 5-9180 and NAG 59167.

REFERENCES

- Ballesteros-Paredes, J., Vázquez-Semadeni, E., & Scalo, J. 1999, *ApJ*, 515, 286
- Ballesteros-Paredes, J., & Mac Low, M.-M. 2002, *ApJ*, 570, 734.
- Barker, D. M. & Mestel, L. 1996, *MNRAS*, 282, 317
- Basu, S. 2000, *ApJ*, 540, L103
- Baureis, P., Ebert, R., & Schmitz, F. 1989, *A&A*, 225, 405
- Beckwith, S. V. W., Sargent, A. I., Chini, R. S., & Güsten, R. 1990, *AJ*, 99, 924
- Bertoldi, F. & McKee, C. F. 1992, *ApJ*, 395, 140
- Burkert, A. & Bodenheimer, P. 2000, *ApJ*, 543, 822
- Crutcher, R. M. 1999, *ApJ*, 520, 706
- Curry, C.L., & McKee, C.F. 2000, *ApJ*, 528, 734
- Curry, C. L. & Stahler, S. W. 2001, *ApJ*, 555, 160
- David, M. & Verschueren, W. 1987, *A&A*, 186, 295
- Evans, C.R., & Hawley, J.F. 1988, *ApJ*, 332, 659
- Fiedler, R. A. & Mouschovias, T. C. 1993, *ApJ*, 415, 680
- Fiege, J. D. & Pudritz, R. E. 2000, *ApJ*, 534, 291
- Fleck, R.C. Jr. 1992, *ApJ*, 401, 146
- Galli, D. & Shu, F.H. 1993, *ApJ*, 417, 243
- Goodman, A. A., Bastien, P., Menard, F., & Myers, P. C. 1990, *ApJ*, 359, 363
- Goodman, A. A., Jones, T. J., Lada, E. A., & Myers, P. C. 1992, *ApJ*, 399, 108
- Goodman, A. A., Benson, P. J., Fuller, G. A., & Myers, P. C. 1993, *ApJ*, 406, 528
- Goodman, A.A., Barranco, J.A., Wilner, D.J., Heyer, M.H. 1998, *ApJ*, 504, 223
- Heiles, C., Goodman, A.A., McKee, C.F., & Zweibel, E.G. 1993, in *Protostars & Planets III* (Arizona: Tucson), 279
- Jones, C.E., Basu, S., & Dubinski, J. 2001, *ApJ*, 551, 387.
- Jones, C.E., & Basu, S. 2002, *ApJ*, 569, 280.
- Juvela, M., Padoan, P., & Nordlund, Å., 2001, *astro-ph/0104280*
- Klessen, R.S. 2001, *ApJ*, 556, 837.
- Klessen, R.S., & Burkert, A. 2001, *ApJ*, 549, 386.
- Li, Z.-Y. & Shu, F. H. 1996, *ApJ*, 472, 211
- Lizano, S. & Shu, F. H. 1989, *ApJ*, 342, 834
- Mac Low, M.-M. 1999, *ApJ*, 524, 169
- Matthews, B. C. & Wilson, C. D. 2000, *ApJ*, 531, 868
- McKee, C. F. & Zweibel, E. G. 1992, *ApJ*, 399, 551
- McLaughlin, D. E. & Pudritz, R. E. 1996, *ApJ*, 469, 194
- Mestel, L. & Ray, T. P. 1985, *MNRAS*, 212, 275
- Mouschovias, T. Ch. 1976, *ApJ*, 207, 141
- Myers, P. C., Dame, T. M., Thaddeus, P., Cohen, R. S., Silverberg, R. F., Dwek, E., & Hauser, M. G. 1986, *ApJ*, 301, 398
- Myers, P. C., Fuller, G. A., Goodman, A. A., & Benson, P. J. 1991, *ApJ*, 376, 561
- Myers, P. C. & Fuller, G. A. 1992, *ApJ*, 396, 631
- Myers, P. C. & Gammie, C. F. 1999, *ApJ*, 522, L141
- Myers, P. C. 1999, *The Physics and Chemistry of the Interstellar Medium*, Proceedings of the 3rd Cologne-Zermatt Symposium, Eds.: V. Ossenkopf, J. Stutzki, and G. Winnewisser, GCA-Verlag Herdecke, 227
- Ohashi, N., Hayashi, M., Ho, P. T. P., Momose, M., Tamura, M., Hirano, N., & Sargent, A. I. 1997, *ApJ*, 488, 317
- Ostriker, E. C., Gammie, C. F., & Stone, J. M. 1999, *ApJ*, 513, 259
- Ostriker, E. C., Stone, J. M., & Gammie, C. F. 2001, *ApJ*, 546, 980
- Ostriker, E.C. 2002, in in "Simulations of magnetohydrodynamic turbulence in astrophysics" Eds. T. Passot & E. Falgarone (Springer Lecture Notes in Physics), *astro-ph/0204463*
- Padoan, P. & Nordlund, Å. 1999, *ApJ*, 526, 279
- Padoan, P., & Nordlund, Å. 2000, *astro-ph/0011229*
- Padoan, P., & Nordlund, Å. 2002, *astro-ph/0205019*
- Padoan, P., Nordlund, Å, Rögnvaldsson, Ö, & Goodman, A. 2000, *astro-ph/0011229*.
- Phelps, R.L., & Lada, E.A. 1997, *ApJ*, 477, 176
- Pichardo, B., Vázquez-Semadeni, E., Gazol, A., Passot, T., Ballesteros-Paredes, J. 2000, *ApJ*, 532, 353
- Ryden, B. S. 1996, *ApJ*, 471, 822
- Simon, M. et al. 1995, *ApJ*, 443, 625
- Stone, J. M., Ostriker, E. C., & Gammie, C. F. 1998, *ApJ*, 508, L99
- Stone, J. M. & Norman, M. L. 1992a, *ApJS*, 80, 753
- Stone, J. M. & Norman, M. L. 1992b, *ApJS*, 80, 791
- Stutzki, J. & Güsten, R. 1990, *ApJ*, 356, 513
- Tomisaka, K., Ikeuchi, S., & Nakamura, T. 1988a, *ApJ*, 326, 208
- Tomisaka, K., Ikeuchi, S., & Nakamura, T. 1988b, *ApJ*, 335, 239
- Truelove, J. K., Klein, R. I., McKee, C. F. Holliman, J. H., II, Howell, L. H. & Greenough, J. A. 1997, *ApJ*, 489, 179
- Williams, J. P. & Blitz, L. 1998, *ApJ*, 494, 657
- Williams, J. P., de Geus, E. J. & Blitz, L. 1994, *ApJ*, 428, 693
- Vázquez-Semadeni, E., Ostriker, E. C., Passot, T., Gammie, C. F., & Stone, J. M. 1998, in "Protostars and Planets IV", Eds. V. Mannings, A. P. Boss, & S. S. Russell, University of Arizona Press.
- Zweibel, E. G. 1990, *ApJ*, 348, 186